Demonstration of a variational quantum eigensolver with a solid-state spin system under ambient conditions

Xuliang Du,[‡] Yang Shen,[‡] Zipeng Wu,[‡] Bei Zeng,[*] and Sen Yang[†]
Department of Physics, The Hong Kong University of Science and Technology, Clear Water Bay, Kowloon, Hong Kong, China

(Received 18 October 2023; revised 24 March 2024; accepted 25 June 2024; published 22 July 2024)

Quantum simulators offer the potential to utilize the quantum nature of a physical system to study another physical system. In contrast to conventional simulation, which experiences an exponential increase in computational complexity, quantum simulation cost increases only linearly with increasing size of the problem, rendering it a promising tool for applications in quantum chemistry. The variational-quantum-eigensolver algorithm is a particularly promising application for investigating molecular electronic structures. For its experimental implementation, spin-based solid-state qubits have the advantage of long decoherence time and high-fidelity quantum gates, which can lead to high accuracy in the ground-state finding. This study uses the nitrogen-vacancy-center system in diamond to implement the variational-quantum-eigensolver algorithm and successfully finds the eigenvalue of a specific Hamiltonian without the need for error-mitigation techniques. With a fidelity of 98.9% between the converged state and the ideal eigenstate, the demonstration provides an important step toward realizing a scalable quantum simulator in solid-state spin systems.

DOI: 10.1103/PhysRevApplied.22.014055

I. INTRODUCTION

Quantum computing has demonstrated its superiority over classical computing in numerous problem domains [1,2], especially in the field of quantum simulation for the study of other physical quantum systems [3]. However, the unavoidable noise from the environment leads to the decoherence of qubits and faulty quantum gates, which restricts further progress in the number of qubits and quantum circuit depth. To counter this, researchers have proposed theories such as quantum error correction to protect quantum systems [4], but their implementation requires a larger number of physical qubits, which in turn introduces more noise [5,6].

Despite the current limitations on the number of qubits available, there are still various algorithms [7] that are capable of leveraging the advantage of quantum systems in this era of so-called noisy intermediate-scale quantum devices [8]. Hybrid quantum-classical algorithms [9] are considered to be promising near-term applications, as they leverage quantum resources to complete classically consumable tasks while leaving other workloads for classical computing resources. The quantum parts of these algorithms often involve variationally updating a parameterized quantum circuit [10], such as the variational quantum eigensolver (VQE) [11–14] and quantum imaginary-time evolution [15,16] for ground-state problems and the quantum approximate optimization algorithm [17].

The VQE is a promising application of quantum simulation in the study of the electronic structures of molecules in quantum chemistry [18]. The energy properties of the molecule are closely related to the ground state of its Hamiltonian. Conventionally, the computational complexity of finding the exact solution of the Hamiltonian increases exponentially with the size of the system. Nonetheless, since qubits evolve by the same nature of quantum mechanics as the electronic wave functions, quantum simulation, as proposed by Feynman [19], can be only linearly costly [20] by simulating a quantum system by another quantum system. This feature makes the VQE a useful tool for computing an upper bound of the Hamiltonian under study.

The experimental implementation of the VQE algorithm presents various challenges due to the requirements for expressibility and entangling capability [21], which necessitate a certain circuit depth. Achieving this circuit depth typically demands a long decoherence time, posing a challenge for experimental realization. Furthermore, the iteration-based and gradient-based optimization process involved in the VQE can be computationally intensive, further adding to the complexity of the experimental

[*]Contact author: zengb@ust.hk
[†]Contact author: phsyang@ust.hk
[‡]These authors contributed equally to this work.

implementation. The first experimental implementation of the VQE was based on a photonic quantum processor [11]. After that, VQE implementations based on ion-trap [22–24], superconducting [25–30], and NMR [31] systems were also realized. Compared with these systems, spin-based solid-state qubits such as the nitrogen-vacancy (N-V)-center spin in diamond offer advantages such as long decoherence time, high-fidelity quantum gates, and less-stringent environmental requirements. However, the suitable ansatz for state preparation and the appropriate methods for state readout and the iteration strategy remain elusive for the implementation of the VQE algorithm on the N-V-center system.

In this work, we use the N-V-center spin in diamond and the nearest-nitrogen nuclear spin to construct the quantum simulator. Although the nitrogen spin is normally a dark spin insensitive to laser illumination, we realize two-qubit readout using the fluorescence-count difference at the excited-state level anticrossing (ESLAC). We choose a hardware-efficient ansatz for generation of the trial state. Without error-mitigation techniques, precise energy estimation is realized by Pauli-term measurements with postrotations after the state preparations. The minimization process to the eigenvalue is observed as the iteration times increase by our optimizing the parameters with the gradient-descent method. The results closely align with the predictions of numerical simulation. The expectation value converges to -2.1, compared with the ideal eigenvalue of $-\sqrt{5}$ (2.236). A fidelity of 98.9% is achieved between the ideal eigenstate and the trial state represented by the converged parameters.

II. VARIATIONAL-QUANTUM-EIGENSOLVER ALGORITHM

A variational algorithm typically involves varying a set of parameters to minimize a defined loss function. For the VQE algorithm, the parameters $\vec{\theta}$ are for the quantum circuit to prepare the state $|\psi(\vec{\theta})\rangle$, which represents an approximation of the ground state of the Hamiltonian under study. The structure of the quantum circuit is defined as the variational ansatz. An effective ansatz not only produces a better approximation of the exact eigenstate but also consumes fewer computing resources.

To investigate the lowest eigenvalue of the Hamiltonian, the loss function is naturally the expectation value

$$E(\vec{\theta}) = \langle\psi(\vec{\theta})|\, H\, |\psi(\vec{\theta})\rangle\,. \tag{1}$$

For the minimization of the expectation value, one can use the gradient-based optimizer in which the gradient is obtained by the parameter-shift rule [32,33]

$$\frac{\partial E(\vec{\theta})}{\partial\theta_i} = (E(\vec{\theta}_i^{+}) - E(\vec{\theta}_i^{-}))/2, \tag{2}$$

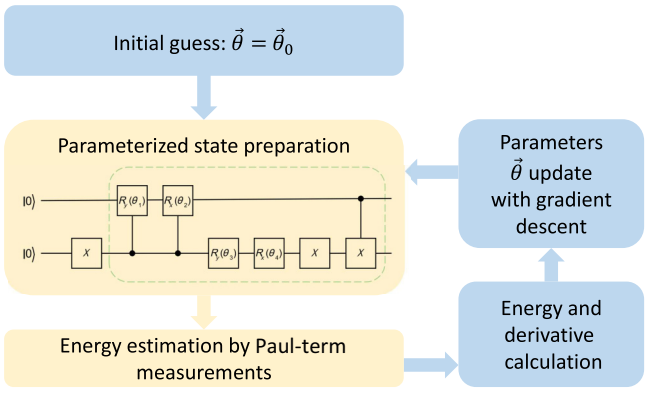

FIG. 1. Procedure for the VQE. The components in yellow use the quantum qubits and the components in pale blue are conducted in a classical computer. The qubit operations in the dashed box are defined as a unit layer in the current quantum circuit.

where $\vec{\theta}_i^{\pm} = \vec{\theta} \pm \frac{\pi}{2}\vec{e}_i$, where $\vec{e}_i$ is the ith unit vector in the parameter space. Thus, the neighboring states in the parameter space are described as $|\psi(\vec{\theta}_i^{\pm})\rangle$. With the gradient, the parameters are updated with use of the gradient-descent method:

$$\vec{\theta}' = \vec{\theta} - \alpha\nabla E(\vec{\theta}). \tag{3}$$

The algorithm distributes the workload between classical and quantum computing resources. It proceeds through a series of steps, as depicted in Fig. 1. A typical iteration of the VQE starts with an initial guess of the parameters $\vec{\theta}$ before the loop begins. According to this set of parameters, a quantum circuit is then used to apply the unitary operation $U(\vec{\theta})$ to the initial state, generating the trial state $|\psi(\vec{\theta})\rangle$. To obtain the gradient information about this set of parameters, states that are nearby in the parameter space are also generated. The states are subsequently measured, and the information about the expectation value of the Hamiltonian is transferred to classical computing resources. The expectation values $\langle\psi(\vec{\theta})|\, H\, |\psi(\vec{\theta})\rangle$ of these states can then be calculated. From these expectation values, the gradients of this set of parameters can also be calculated. The parameters are updated with use of the gradient-descent method, and a new iteration begins with the updated parameters. The loop continues until the expectation value converges to the minimum.

III. EXPERIMENTAL IMPLEMENTATION

The VQE algorithm is implemented on a two-qubit system composed of the N-V-center spin and the nitrogen nuclear spin. The negatively charged N-V center is a form of point defect in diamond that acts as a spin-1 system [34,35]. The N-V center has a long coherence time [36], making it a favorable option for realizing a quantum simulator. The naturally occurring nitrogen nuclear spin of the

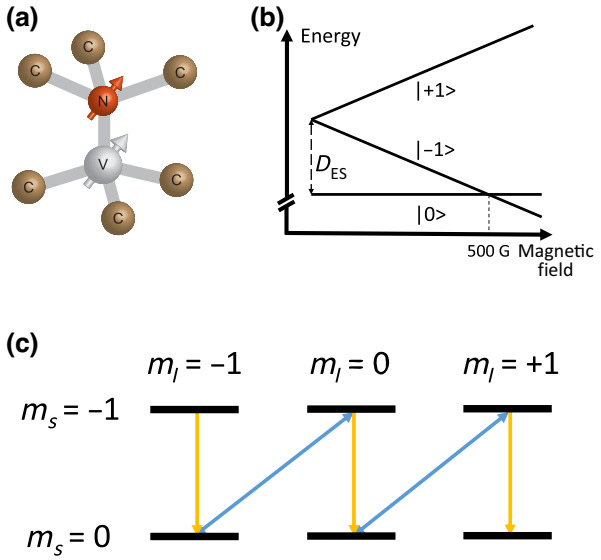

FIG. 2. Experimental system for the VQE. (a) The N-V-center spin and nitrogen nuclear spin as qubits. (b) Spin energy levels in excited states for various magnetic fields. The $|m_s = 0\rangle$ and $|m_s = -1\rangle$ states cross at around 500 G, causing ESLAC. (c) Optical initialization at the ESLAC. The strong hyperfine coupling between the electron spin and the nuclear spin enables the energy-conserving flip-flop process between them. Yellow single-headed arrows mean laser initialization of the N-V-center spin to the $|m_s = 0\rangle$ state and purple double-headed arrows characterize the flip-flop process.

N-V center can be coupled to it with hyperfine interaction, forming a two-qubit system. A schematic illustration of the two-qubit system of the N-V-center spin and the nitrogen nuclear spin is shown in Fig. 2(a). The details of our experimental setup are discussed in Appendix A. Our implementation of the VQE algorithm uses the $m_s = 0$ and $m_s = -1$ subspace of the N-V center and the $m_I = +1$ and $m_I = 0$ subspace of the nitrogen nucleus to define the qubits. m_s is the magnetic quantum number of the electron spin and m_I is the magnetic quantum number of the nitrogen nuclear spin. In this paper, we designate the nitrogen nuclear spin as qubit 1, with parameters θ_1 and θ_2 for y and x rotations as in the quantum circuit in Fig. 1. Likewise, the N-V-center spin is identified as qubit 2, with parameters θ_3 and θ_4. We carefully selected the four parameters in a way that each spin possesses two degrees of freedom. This decision was made on the basis of our prior knowledge of the Hamiltonian, allowing us to effectively represent its solution space while minimizing the number of gates required. We set the magnetic field to around 500 G to reach the ESLAC, with which we can initialize the system by optical illumination [37] as shown in Figs. 2(b) and 2(c). The ESLAC-caused spin-dependent fluorescence is also the key to reading out the system [38]. The coherent control of the N-V-center electron spin and nitrogen nuclear spin is realized by our applying microwave and radio-frequency pulses.

The Hamiltonian under study is

$$H = X_1X_2 + Z_1 + Z_2. \tag{4}$$

The minimum eigenvalue of this Hamiltonian should be $-\sqrt{5}$, and it corresponds to the eigenstate $-\sqrt{50 - 20\sqrt{5}}/10\,|00\rangle + \sqrt{50 + 20\sqrt{5}}/10\,|11\rangle$. Although it is obvious that the straightforward Pauli measurements are X_1X_2, I_1Z_2, and Z_1I_2, measurements of I_1I_2, I_1Z_2, Z_1I_2, Z_1Z_2, $X_1X_2 + Y_1Y_2$, and $X_1X_2 - Y_1Y_2$ are needed in our experiments due to the restriction of the N-V-center system, which is discussed in detail in Appendices B and C.

The experimental procedure for the VQE can be summarized as the following steps:

(1) *Choose an initial guess of the parameters* $\vec{\theta}_0$ *and an appropriate learning rate* α. The four components of $\vec{\theta}_0$ correspond, respectively, to the nuclear and electron spin rotation angles in the y and x directions. The learning rate α for the updating of the parameters can affect both the optimization process and the final expectation value the process converges to. An appropriate learning rate is expected to be small enough to cause convergence close to the ideal eigenvalue but will not make the convergence process too slow. The closeness also reaches a plateau when α is below a certain value.

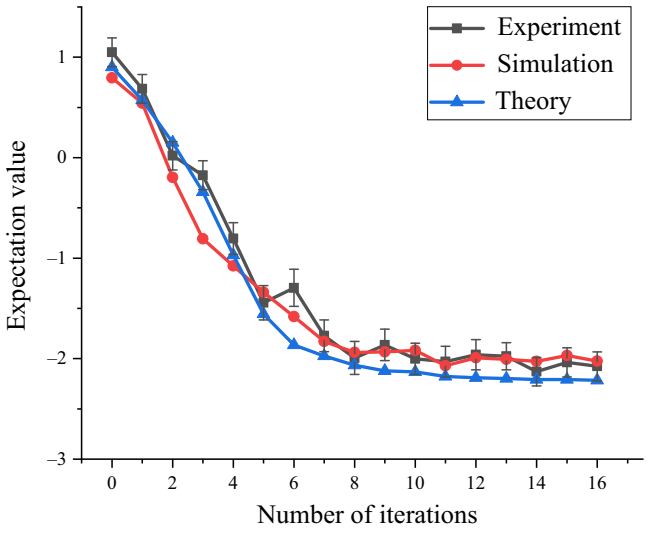

FIG. 3. Minimization process for the expectation value during VQE iterations. The brown line represents the experimental result. The orange line represents the simulated minimization process with the same initial guess and learning rate. The specific parameters for each iteration in the simulation line are calculated according to the simulation result for the last iteration, different from the experimental parameters. The blue line represents the theoretical expectation value for the same set of parameters in the experiment for each iteration.

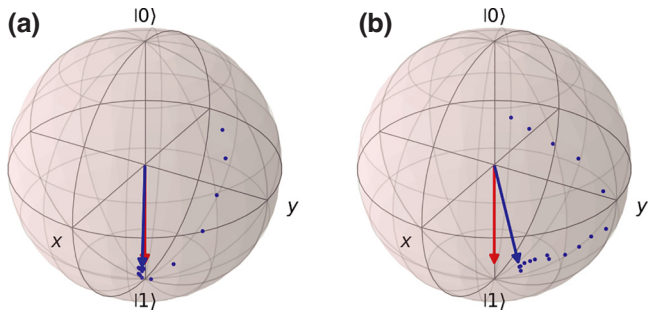

FIG. 4. Minimization process in a Bloch sphere of (a) the nitrogen nuclear spin qubit and (b) the N-V-center spin qubit. The red arrow represents the ideal eigenstate and the blue arrow represents the state of the converged parameters. The blue dots represent the state of the parameters in different iterations.

(2) *Prepare and measure the quantum states.* The trial state $|\psi(\vec{\theta})\rangle$ is prepared with the hardware-efficient ansatz depicted in Fig. 1, in which θ_i, representing the rotation angle, is encoded as the duration of a driving pulse in hardware. In this paper, we use one layer in the state preparation to generate the trial state. By postrotations after the state preparation, measurements of certain Pauli matrices are achieved. According to the specific Hamiltonian, we can choose the specific Pauli terms to measure. The preparation and the readout are also repeated for eight other, neighboring states $|\psi(\vec{\theta}_i^{\pm})\rangle$ in the parameter space. In the course of experimentation, it is imperative to execute a particular sequence for a given state repeatedly for a significant number of instances to ensure reliability and precision of the results obtained. In this regard, it is noteworthy that 10^6 trials are conducted for each sequence corresponding to a single state in our experiment.

(3) *Estimate the expectation values and the gradients.* The expectation values are calculated on a classical computer with the results of Pauli measurements on a quantum computer for the trial state and eight neighboring states. The four gradients of the expectation value in $\vec{\theta}_0$ are calculated by the parameter-shift rule [Eq. (2)] with the estimated expectation values of eight neighboring states.

(4) *Update the parameters.* The parameters are updated with us eof the gradient-descent method [Eq. (3)] with the four gradients calculated in step (4).

(5) *Repeat steps (2)–(4) until the expectation value converges to the minimum.*

We start the VQE experiment with a random initial guess of the parameters as $\vec{\theta}_0 = (0.1, 0.2, 0.1, 0.2) \times 2\pi$. To reduce the duration of the experiment without compromising the optimization intricacies, the learning rate α is set to 0.3. The algorithm converges to $E(\vec{\theta}) \approx -2.1$ after 16 iterations as shown in Fig. 3 as the brown line. The trial state represented by the converged parameters has a

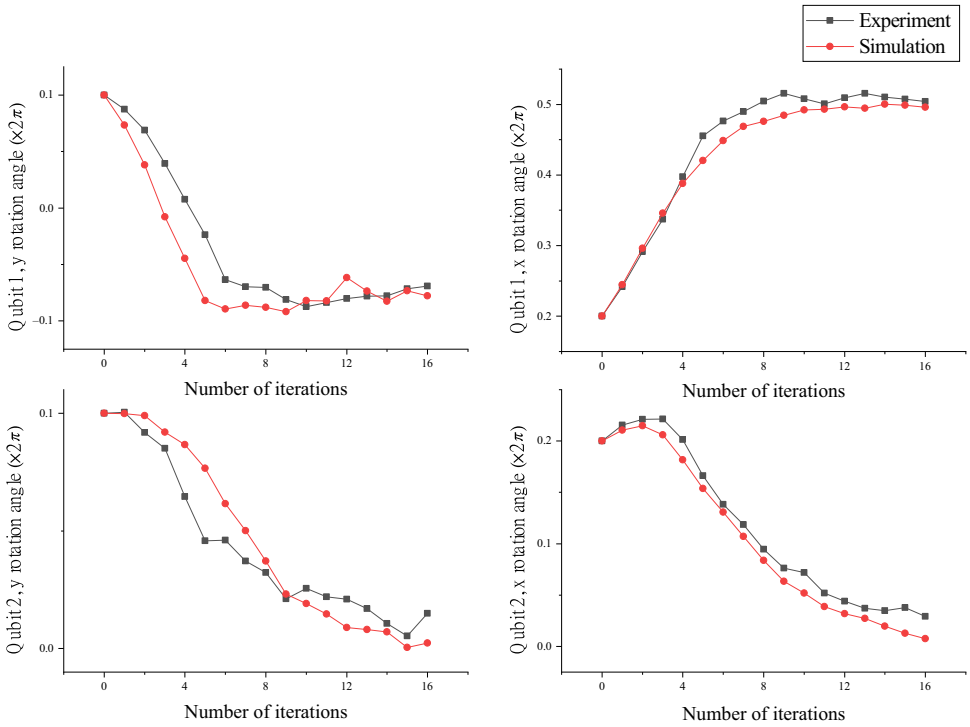

FIG. 5. Specific optimization processes for four specific parameters. The four plots correspond to the nuclear (qubit 1) and electron (qubit 2) spin rotation angles in the y and x directions, respectively. The brown line represents the experimental result. The orange line represents the simulated minimization process with the same initial guess and learning rate.

fidelity of 98.9% with the ideal eigenstate. The trajectories in the Bloch sphere of the minimization process for two spins are depicted as the blue dots in Fig. 4. The dots in the Bloch spheres represent the reduced density matrices of two spins. For the specific optimization processes for four parameters, experimental and simulation results are included in Fig. 5. From the optimization processes for the parameters of the electron spin qubit, we can infer that more iterations may eliminate the distance between the converged state and the ideal eigenstate of the N-V-center spin qubit in Fig. 4.

By comparison with the simulations in QISKIT [39], we find that the method based on Pauli-term measurements to estimate the expectation value has a readout error with a magnitude of approximately 0.01, which is discussed in detail in Appendix E. The major noise contributing to the fluctuation of the measured expectation value is photon shot noise. Although the percentage error of the fluorescence count reaches 0.1% as a result of 10^6 repetitions for each state, the fluctuation of the final calculated value is larger due to the error propagation. Besides, the inhomogeneity of the magnetic field in different runs of the experiment and the error of the fitted resonance frequency affect not only the precision of the estimation of the expectation value but also the generation of the desired state, causing the difference between the VQE-optimized expectation value and the ideal eigenvalue. After estimating the magnitude of the dephasing process through T_2^* experiments, we add the above-mentioned noise and simulate the experiment in the Lindblad equation with QuTiP [40,41] using the same initial guess of the parameters, learning rate, and other experimental parameters, which is discussed in detail in Appendix D and shown in Fig. 3. The estimation of the error bar in the experimental result is accomplished through a method inspired by the Monte Carlo experiment. More specifically, the method involves the random sampling of direct measurement outcome errors, which are based on their corresponding experimental photon shot noise. Subsequently, the error-added results go through normal data processing, resulting in the generation of a distribution for the expectation value. The error bar is then defined as the standard deviation of this distribution.

IV. CONCLUSION

We demonstrate the variational-quantum-eigensolver algorithm on a two-qubit system based on the nitrogen-vacancy center in diamond under ambient conditions. A decay to the lowest eigenvalue for the Hamiltonian under study is observed as predicted by the numerical simulation with our noise model. The accuracy can be further increased by uss of optimal control [42] and error-mitigation techniques.

Although only a simple VQE algorithm with four parameters is implemented in this work, the simulation power can be broadened by one leveraging all three levels of the N-V-center spin and nitrogen nuclear spin to construct a quantum simulator of two qutrits. In addition to the VQE, other quantum-classical algorithms, such as the quantum approximate optimization algorithm, can also benefit from this qutrit system [43]. The initialization-and-readout method can be generalized from the existing technique based on the ESLAC. Besides, more layers in the parameterized state preparation can be added to increase the expressibility and entangling capability [21].

Furthermore, the demonstration has substantial scalability and versatility for extension to other fields of solid-spin systems. To scale up the system, besides using nuclear spin qubits around the color center [44,45], we can also develop a connected network of entangled nodes, each containing a limited number of qubits [46]. The coupling between nodes has been realized on N-V centers [47] and group-IV vacancies in diamond [48]. This can help the VQE to study more-complex Hamiltonians or harness parallelism to accelerate the optimization process [49]. Moreover, we demonstrate the feasibility of implementing the VQE on hybrid spin systems, where coherent control and readout present challenges due to the distinct spin species and one spin functioning as a readout probe. Our approach to this issue and the entangled-node architecture can be extended to other solid-state hybrid spin platforms with a similar problem, such as group-IV vacancies in diamond, rare-earth ions in solids [50], and divacancies in silicon carbide [51]. Besides, our Pauli-measurement technique is essentially an efficient two-qubit tomography method, which can be adapted for other quantum applications, such as quantum sensing.

ACKNOWLEDGMENTS

We thank Cheuk Kit Cheung for fruitful discussion. B.Z. acknowledges financial support from Hong Kong RGC (Grant No. GRF/16305121). S.Y. acknowledges financial support from Hong Kong RGC (Grant No. GRF/16305422).

APPENDIX A: EXPERIMENTAL SETUP

The experimental configuration is illustrated in Fig. 6. We use a type-IIa-natural-diamond sample oriented along the 111 crystallographic direction with a 1.1% natural abundance of ^{13}C. The diamond sample is affixed to a sample holder, which has a copper wire located near the N-V center and is connected to the microwave-and-radio-frequency system. To increase the collection efficiency, a solid immersion lens is fabricated around the N-V center with use of a focused ion beam. Additionally, a permanent magnet is situated close to the sample to create a magnetic field parallel to the N-V axis.

The green laser light used for N-V-center initialization is generated with a 530 nm laser source (Coherent

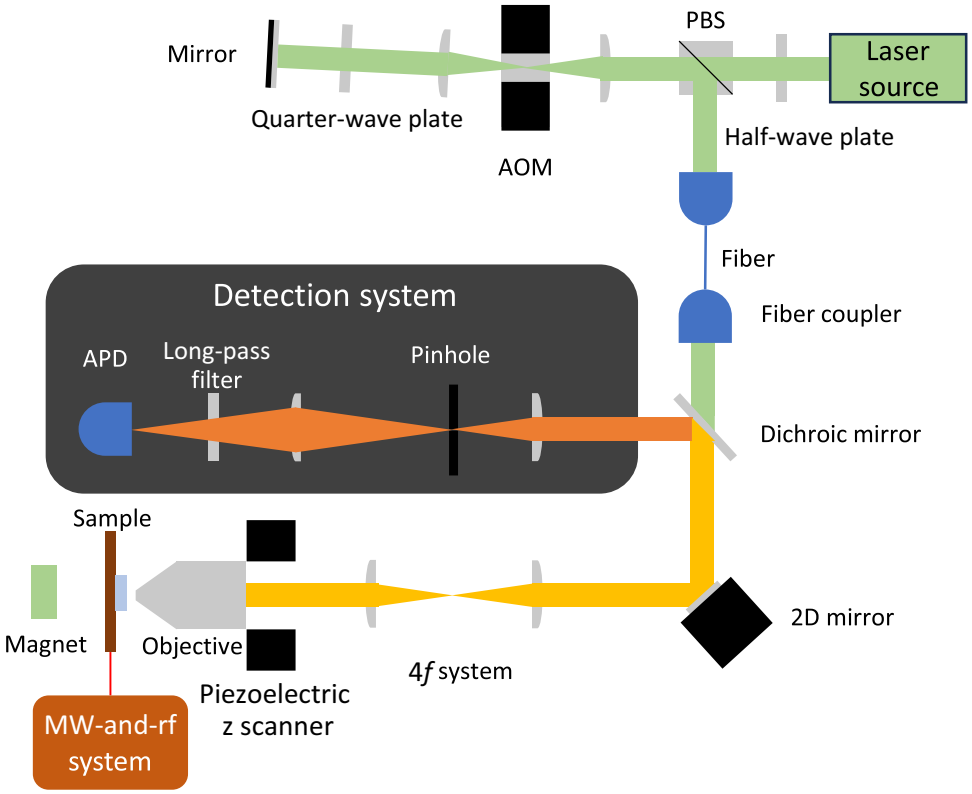

FIG. 6. Experimental setup. AOM, acousto-optic modulator; APD, avalanche photon detector; MW, microwave; PBS, polarizing beam splitter; rf, radio frequency.

Sapphire) and is subsequently directed through a half-wave plate to modify the polarization direction. Then it first passes through a polarizing beam splitter. After double passing through an acousto-optic modulator (Gooch & Housego 3350-199) and a quarter-wave plate altering the polarization, the laser light is reflected by the polarizing beam splitter with a polarization perpendicular to the original polarization and coupled into a fiber. The acousto-optic modulator, which can function as a switch for the green laser, is controlled by 350-MHz microwave pulses. After exiting the fiber, the green laser light passes through a dichroic mirror and is reflected by a piezoelectric-controlled 2D mirror before entering the $4f$ system, which includes two additional lenses. The 2D mirror enables an x-y-plane scan of the diamond sample. Following the second lens, the green light is directed into an oil $\times 100$ objective (UPLSAPO100XO) with a numerical aperture of 1.4 mounted on the piezoelectric z scanner. Finally, the laser light reaches the N-V center, and the z scanner controls the objective's z position, enabling a z-direction scan of the diamond sample.

The red fluorescence emitted by the N-V center propagates back along the same optical path as the green laser light until it reaches the dichroic mirror, where it is reflected toward the detection system. The lens and the pinhole work like a spatial filter of fluorescence. After the pinhole, a long-pass filter is used to further filter out non-fluorescence photons. Finally, the fluorescence is focused into an avalanche photon detector (SPCM-AQRH-10-FC, Excelitas Technologies).

APPENDIX B: PAULI MEASUREMENTS

Pauli measurements after the trial-state preparation are based on the different photoluminescence rates of different states under the condition of the ESLAC [38,52]. Figure 7 shows the typical time-binned photoluminescence of the N-V-nitrogen two-qubit system in different states. Since the photoluminescence of an arbitrary state depends simply on its population in different states, the measurement matrix without postrotation is simply

$$M_0 = \begin{pmatrix} N_1 & 0 & 0 & 0 \\ 0 & N_2 & 0 & 0 \\ 0 & 0 & N_3 & 0 \\ 0 & 0 & 0 & N_4 \end{pmatrix}, \tag{B1}$$

in which N is the photoluminescence count and 1, 2, 3, and 4 denote the states $|0,+1\rangle$, $|0,0\rangle$, $|-1,+1\rangle$, and $|-1,0\rangle$, respectively.

To realize Pauli measurements I_1I_2, I_1Z_2, Z_1I_2, and Z_1Z_2, we also perform the measurements with the postrotation of

π pulses between these states. By doing this, we realize the measurement matrices

$$M_{\pi_{13}} = \begin{pmatrix} N_3 & 0 & 0 & 0 \\ 0 & N_2 & 0 & 0 \\ 0 & 0 & N_1 & 0 \\ 0 & 0 & 0 & N_4 \end{pmatrix}, \tag{B2}$$

$$M_{\pi_{34}} = \begin{pmatrix} N_1 & 0 & 0 & 0 \\ 0 & N_2 & 0 & 0 \\ 0 & 0 & N_4 & 0 \\ 0 & 0 & 0 & N_3 \end{pmatrix}, \tag{B3}$$

$$M_{\Pi} = \begin{pmatrix} N_3 & 0 & 0 & 0 \\ 0 & N_4 & 0 & 0 \\ 0 & 0 & N_1 & 0 \\ 0 & 0 & 0 & N_2 \end{pmatrix}, \tag{B4}$$

in which $M_{\pi_{13}}$ means a π pulse between states $|0,+1\rangle$ and $|-1,+1\rangle$ is applied after the trial-state preparation and before the photon-count measurement. $M_{\pi_{34}}$ corresponds to a π pulse between states $|-1,0\rangle$ and $|-1,+1\rangle$ and M_{Π} corresponds to a hard π pulse that flips both $|0,+1\rangle \longleftrightarrow |-1,+1\rangle$ and $|0,0\rangle \longleftrightarrow |-1,0\rangle$.

With the results of M_0, $M_{\pi_{13}}$, $M_{\pi_{34}}$, and M_{Π} as R_0, $R_{\pi_{13}}$, $R_{\pi_{34}}$, and R_{Π}, we get the Pauli-measurement results

$$\begin{pmatrix} R_{I_1I_2} \\ R_{I_1Z_2} \\ R_{Z_1I_2} \\ R_{Z_1Z_2} \end{pmatrix} = \begin{pmatrix} 1 & 1 & 1 & 1 \\ 1 & -1 & 1 & -1 \\ 1 & 1 & -1 & -1 \\ 1 & -1 & -1 & 1 \end{pmatrix} \begin{pmatrix} N_1 & N_2 & N_3 & N_4 \\ N_3 & N_2 & N_1 & N_4 \\ N_1 & N_2 & N_4 & N_3 \\ N_3 & N_4 & N_1 & N_2 \end{pmatrix}^{-1} \begin{pmatrix} R_0 \\ R_{\pi_{13}} \\ R_{\pi_{34}} \\ R_{\Pi} \end{pmatrix}. \tag{B5}$$

To realize the Pauli measurement of X_1X_2, we have to perform the measurement of both $X_1X_2 + Y_1Y_2$ and $X_1X_2 - Y_1Y_2$. The $X_1X_2 + Y_1Y_2$ term is measured by our considering the photoluminescence difference between two sequences with postrotations. The difference is normalized by the difference between the states $|0,+1\rangle$ and $|-1,0\rangle$. The first sequence consists of a π pulse between the states $|0,+1\rangle$ and $|-1,+1\rangle$, followed by a $\pi/2$ pulse around the y axis of the nitrogen nuclear spin in the rotating frame between the states $|-1,+1\rangle$ and $|-1,0\rangle$, and finally another π pulse between the states $|0,+1\rangle$ and $|-1,+1\rangle$.

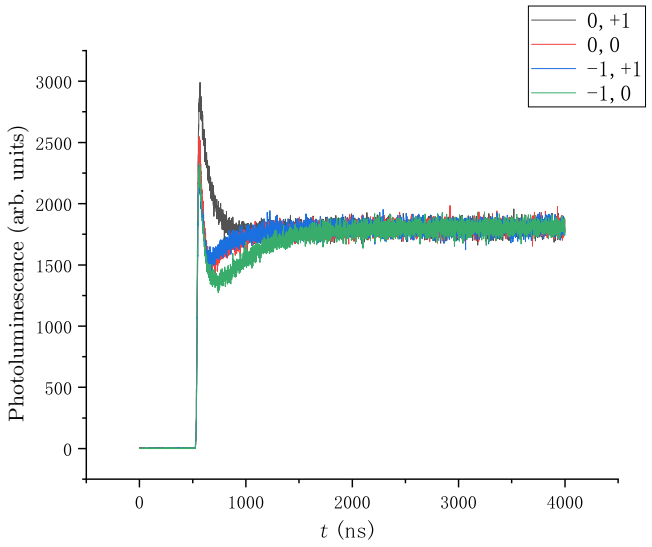

FIG. 7. Typical time-binned photoluminescence of different states.

The second sequence is identical, except for an opposite rotation around the $-y$ axis for the second pulse. The $X_1X_2 - Y_1Y_2$ term is measured in the same way but the first pulse for the two sequences is a π pulse between the states $|0,0\rangle$ and $|-1,0\rangle$. The quantum circuits of the postrotations for the measurement of $X_1X_2 + Y_1Y_2$ and $X_1X_2 - Y_1Y_2$ are shown in Fig. 8.

APPENDIX C: PHASE CONSIDERATION IN THE QUANTUM CIRCUIT

Owing to the limited power of microwaves, it is crucial to account for the unavoidable duration time of the quantum gate imposed on the electron spin when one is conducting the in-phase measurement of the nuclear spin. Throughout the operation of the quantum gate, the electron spin is in a superposition state of $|0\rangle$ and $|-1\rangle$. Given the intimate connection between the nuclear and electron spins, facilitated primarily by the hyperfine interaction, differing states of the electron spin can result in disparate energy splittings between the up and down states of the nuclear spin. Consequently, the nuclear spin undergoes precession around the direction of the magnetic field with a frequency that is contingent on the state of the electron spin. For the purpose of manipulating the nuclear spin within the rotating frame, one must contemplate the phase discrepancy induced by this disparity in frequency.

All radio-frequency pulses used for the manipulation of the nuclear spin are in resonance with the transition between the $|-1,+1\rangle$ and $|-1,0\rangle$ states. Hence, we opt to probe the nuclear spin in this particular rotating frame. Nevertheless, the parameters θ_3 and θ_4 imply that part

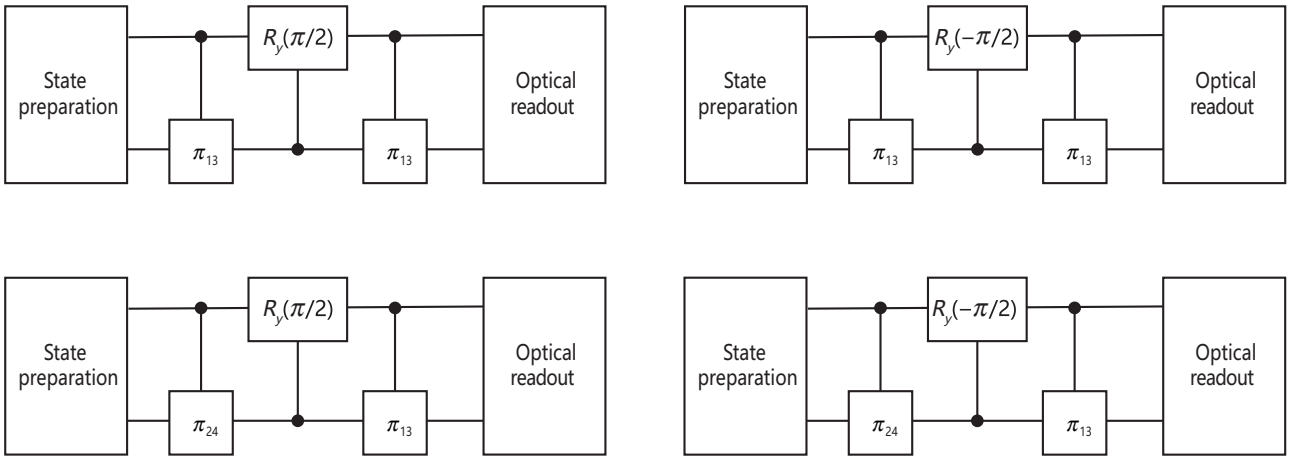

FIG. 8. Quantum circuits of the postrotations for the measurement of $X_1X_2 + Y_1Y_2$ and $X_1X_2 - Y_1Y_2$.

of the electron spin's population will undergo rotation towards and back from the state $|0\rangle$ on application of microwave pulses. Within the previously stated rotating frame, the nuclear spin will precess at a frequency of 2.16 MHz (the hyperfine interaction strength) when the electron spin is in the state $|0\rangle$. It thus follows that the phase of the measurement gates for the nuclear spin, subsequent to the preparation of the trial state, requires modification after the process through the state $|0\rangle$. Besides, the measurement result also needs to be modified because of the phase spreading during the process. Through the simulation of the dynamics under the influence of microwave pulses directly using Schrodinger's equation with QuTiP [40,41], we derive the phase discrepancy for the radio-frequency pulse in the postrotation sequences and the correction factor for the readout results.

APPENDIX D: SIMULATION

A common method to describe the dynamics of a system interacting with the environment is the use of the Lindblad master equation, which has the form

$$\dot{\rho}(t) = -\frac{i}{\hbar}[H(t), \rho(t)] + \sum_n \frac{1}{2}[2C_n\rho(t)C_n^\dagger - \rho(t)C_n^\dagger C_n - C_n^\dagger C_n\rho(t)], \tag{D1}$$

where C_n is the collapse operator characterizing the influence of the environment. Since the dephasing process caused by the inhomogeneity of the magnetic field plays a major role in decoherence in our experiment, we consider mainly the collapse operator with the form

$$C_n = \begin{pmatrix} 0 & 0 \\ 0 & 1 \end{pmatrix}. \tag{D2}$$

Through the T_2^* measurement shown in Fig. 9, we estimate that T_2^* is around 4.367 μs, from which we can estimate the amplitude of the collapse operator.

With knowledge of the decoherence and specific experimental parameters, we next use the Lindblad equation in QuTiP to compute the dynamics of the two-qubit system under the microwave and radio-frequency driving in each experimental sequence. To account for photon shot noise, we introduce white noise with magnitude equivalent to that of experimental signal. The simulated outcomes then go through the same data-processing procedures as the experimental data, yielding the simulated expectation value for a specific parameter set. In the simulation results, only the initial point shares the same parameters as the experiment, while all subsequent iteration points are generated on the basis of the gradients calculated with use of the expectation value obtained during the simulation.

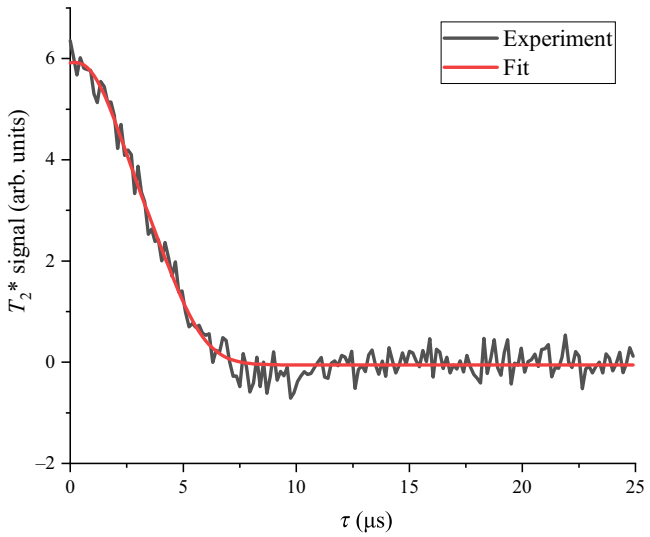

FIG. 9. T_2^* measurement with experimental data and the fit.

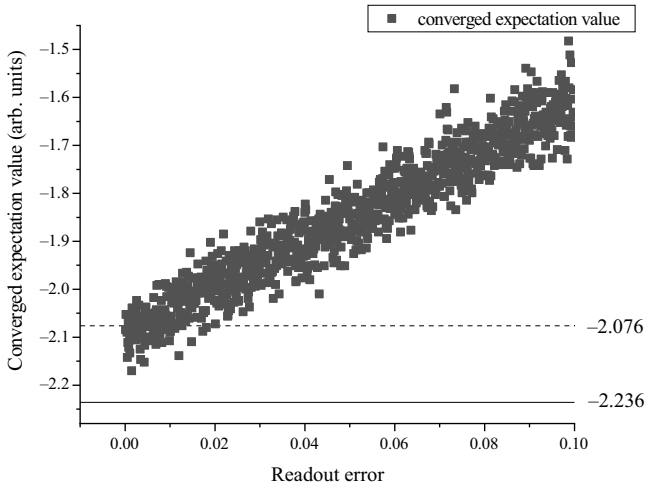

FIG. 10. Relation between the converged expectation value and readout error.

APPENDIX E: CONVERGED EXPECTATION VALUE AND READOUT ERROR

To study the readout error of our method based on Pauli-term measurements, we simulate the VQE iterations with different readout errors in QISKIT [39]. The iteration times, initial guess, learning rate, and gate fidelity are set near the experimental values. The final converged expectation value (and the distance from the true value) is found to have a positive correlation with the readout error as illustrated in Fig. 10. Since our converged minimum is −2.076, we can infer from Fig. 10 that the readout error of our method is approximately of magnitude 0.01.

[1] P. W. Shor, in *Proceedings 35th Annual Symposium on Foundations of Computer Science* (IEEE, Santa Fe, NM, USA, 1994), p. 124.

[2] L. K. Grover, Quantum mechanics helps in searching for a needle in a haystack, Phys. Rev. Lett. **79**, 325 (1997).

[3] Y. Cao, J. Romero, J. P. Olson, M. Degroote, P. D. Johnson, M. Kieferová, I. D. Kivlichan, T. Menke, B. Peropadre, N. P. Sawaya *et al.*, Quantum chemistry in the age of quantum computing, Chem. Rev. **119**, 10856 (2019).

[4] M. A. Nielsen and I. L. Chuang, *Quantum Computation and Quantum Information* (Cambridge University Press, Cambridge, 2010).

[5] D. G. Cory, M. Price, W. Maas, E. Knill, R. Laflamme, W. H. Zurek, T. F. Havel, and S. S. Somaroo, Experimental quantum error correction, Phys. Rev. Lett. **81**, 2152 (1998).

[6] Google Quantum AI, Suppressing quantum errors by scaling a surface code logical qubit, Nature **614**, 676 (2023).

[7] K. Bharti, A. Cervera-Lierta, T. H. Kyaw, T. Haug, S. Alperin-Lea, A. Anand, M. Degroote, H. Heimonen, J. S. Kottmann, T. Menke *et al.*, Noisy intermediate-scale quantum algorithms, Rev. Mod. Phys. **94**, 015004 (2022).

[8] J. Preskill, Quantum computing in the NISQ era and beyond, Quantum **2**, 79 (2018).

[9] S. Endo, Z. Cai, S. C. Benjamin, and X. Yuan, Hybrid quantum-classical algorithms and quantum error mitigation, J. Phys. Soc. Japan **90**, 032001 (2021).

[10] M. Cerezo, A. Arrasmith, R. Babbush, S. C. Benjamin, S. Endo, K. Fujii, J. R. McClean, K. Mitarai, X. Yuan, L. Cincio *et al.*, Variational quantum algorithms, Nat. Rev. Phys. **3**, 625 (2021).

[11] A. Peruzzo, J. McClean, P. Shadbolt, M.-H. Yung, X.-Q. Zhou, P. J. Love, A. Aspuru-Guzik, and J. L. O'Brien, A variational eigenvalue solver on a photonic quantum processor, Nat. Commun. **5**, 4213 (2014).

[12] J. R. McClean, J. Romero, R. Babbush, and A. Aspuru-Guzik, The theory of variational hybrid quantum-classical algorithms, New J. Phys. **18**, 023023 (2016).

[13] J. Tilly, H. Chen, S. Cao, D. Picozzi, K. Setia, Y. Li, E. Grant, L. Wossnig, I. Rungger, G. H. Booth *et al.*, The variational quantum eigensolver: A review of methods and best practices, Phys. Rep. **986**, 1 (2022).

[14] D. A. Fedorov, B. Peng, N. Govind, and Y. Alexeev, VQE method: A short survey and recent developments, Mater. Theory **6**, 1 (2022).

[15] M. Motta, C. Sun, A. T. Tan, M. J. O'Rourke, E. Ye, A. J. Minnich, F. G. Brandao, and G. K.-L. Chan, Determining eigenstates and thermal states on a quantum computer using quantum imaginary time evolution, Nat. Phys. **16**, 205 (2020).

[16] S. McArdle, T. Jones, S. Endo, Y. Li, S. C. Benjamin, and X. Yuan, Variational ansatz-based quantum simulation of imaginary time evolution, npj Quantum Inf. **5**, 75 (2019).

[17] E. Farhi, J. Goldstone, and S. Gutmann, A quantum approximate optimization algorithm, arXiv:1411.4028.

[18] S. McArdle, S. Endo, A. Aspuru-Guzik, S. C. Benjamin, and X. Yuan, Quantum computational chemistry, Rev. Mod. Phys. **92**, 015003 (2020).

[19] R. P. Feynman *et al.*, Simulating physics with computers, Int. J. Theor. Phys. **21**, 467 (2018).

[20] D. W. Berry, G. Ahokas, R. Cleve, and B. C. Sanders, Efficient quantum algorithms for simulating sparse Hamiltonians, Commun. Math. Phys. **270**, 359 (2007).

[21] S. Sim, P. D. Johnson, and A. Aspuru-Guzik, Expressibility and entangling capability of parameterized quantum circuits for hybrid quantum-classical algorithms, Adv. Quantum Technol. **2**, 1900070 (2019).

[22] C. Hempel, C. Maier, J. Romero, J. McClean, T. Monz, H. Shen, P. Jurcevic, B. P. Lanyon, P. Love, R. Babbush *et al.*, Quantum chemistry calculations on a trapped-ion quantum simulator, Phys. Rev. X **8**, 031022 (2018).

[23] Y. Nam, J.-S. Chen, N. C. Pisenti, K. Wright, C. Delaney, D. Maslov, K. R. Brown, S. Allen, J. M. Amini, J. Apisdorf *et al.*, Ground-state energy estimation of the water molecule on a trapped-ion quantum computer, npj Quantum Inf. **6**, 33 (2020).

[24] L. Zhao, J. Goings, K. Shin, W. Kyoung, J. I. Fuks, J.-K. Kevin Rhee, Y. M. Rhee, K. Wright, J. Nguyen, J. Kim *et al.*, Orbital-optimized pair-correlated electron simulations on trapped-ion quantum computers, npj Quantum Inf. **9**, 60 (2023).

[25] P. J. O'Malley, R. Babbush, I. D. Kivlichan, J. Romero, J. R. McClean, R. Barends, J. Kelly, P. Roushan, A. Tranter,

N. Ding *et al.*, Scalable quantum simulation of molecular energies, Phys. Rev. X **6**, 031007 (2016).

[26] A. Kandala, A. Mezzacapo, K. Temme, M. Takita, M. Brink, J. M. Chow, and J. M. Gambetta, Hardware-efficient variational quantum eigensolver for small molecules and quantum magnets, Nature **549**, 242 (2017).

[27] A. J. McCaskey, Z. P. Parks, J. Jakowski, S. V. Moore, T. D. Morris, T. S. Humble, and R. C. Pooser, Quantum chemistry as a benchmark for near-term quantum computers, npj Quantum Inf. **5**, 99 (2019).

[28] F. Arute, K. Arya, R. Babbush, D. Bacon, J. C. Bardin, R. Barends, S. Boixo, M. Broughton, B. B. Buckley, D. A. Buell *et al.*, Hartree-Fock on a superconducting qubit quantum computer, Science **369**, 1084 (2020).

[29] S. Stanisic, J. L. Bosse, F. M. Gambetta, R. A. Santos, W. Mruczkiewicz, T. E. O'Brien, E. Ostby, and A. Montanaro, Observing ground-state properties of the Fermi-Hubbard model using a scalable algorithm on a quantum computer, Nat. Commun. **13**, 5743 (2022).

[30] B. Huang, M. Govoni, and G. Galli, Simulating the electronic structure of spin defects on quantum computers, PRX Quantum **3**, 010339 (2022).

[31] S.-Y. Hou, G. Feng, Z. Wu, H. Zou, W. Shi, J. Zeng, C. Cao, S. Yu, Z. Sheng, X. Rao *et al.*, SpinQ Gemini: A desktop quantum computing platform for education and research, EPJ Quantum Technol. **8**, 1 (2021).

[32] M. Schuld, V. Bergholm, C. Gogolin, J. Izaac, and N. Killoran, Evaluating analytic gradients on quantum hardware, Phys. Rev. A **99**, 032331 (2019).

[33] K. Mitarai, M. Negoro, M. Kitagawa, and K. Fujii, Quantum circuit learning, Phys. Rev. A **98**, 032309 (2018).

[34] M. W. Doherty, N. B. Manson, P. Delaney, and L. C. Hollenberg, The negatively charged nitrogen-vacancy centre in diamond: the electronic solution, New J. Phys. **13**, 025019 (2011).

[35] F. Jelezko and J. Wrachtrup, Single defect centres in diamond: A review, Phys. Status Solidi (a) **203**, 3207 (2006).

[36] E. Herbschleb, H. Kato, Y. Maruyama, T. Danjo, T. Makino, S. Yamasaki, I. Ohki, K. Hayashi, H. Morishita, M. Fujiwara *et al.*, Ultra-long coherence times amongst room-temperature solid-state spins, Nat. Commun. **10**, 3766 (2019).

[37] V. Jacques, P. Neumann, J. Beck, M. Markham, D. Twitchen, J. Meijer, F. Kaiser, G. Balasubramanian, F. Jelezko, and J. Wrachtrup, Dynamic polarization of single nuclear spins by optical pumping of nitrogen-vacancy color centers in diamond at room temperature, Phys. Rev. Lett. **102**, 057403 (2009).

[38] T. Van der Sar, Z. Wang, M. Blok, H. Bernien, T. Taminiau, D. Toyli, D. Lidar, D. Awschalom, R. Hanson, and V. Dobrovitski, Decoherence-protected quantum gates for a hybrid solid-state spin register, Nature **484**, 82 (2012).

[39] A. Javadi-Abhari, M. Treinish, K. Krsulich, C. J. Wood, J. Lishman, J. Gacon, S. Martiel, P. D. Nation, L. S. Bishop, A. W. Cross, *et al.*, Quantum computing with Qiskit, arXiv:2405.08810.

[40] J. Johansson, P. Nation, and F. Nori, QuTiP: An open-source Python framework for the dynamics of open quantum systems, Comput. Phys. Commun. **183**, 1760 (2012).

[41] J. Johansson, P. Nation, and F. Nori, QuTiP 2: A Python framework for the dynamics of open quantum systems, Comput. Phys. Commun. **184**, 1234 (2013).

[42] X. Rong, J. Geng, F. Shi, Y. Liu, K. Xu, W. Ma, F. Kong, Z. Jiang, Y. Wu, and J. Du, Experimental fault-tolerant universal quantum gates with solid-state spins under ambient conditions, Nat. Commun. **6**, 8748 (2015).

[43] G. Bottrill, M. Pandey, and O. Di Matteo, in *2023 IEEE International Conference on Quantum Computing and Engineering (QCE)* (IEEE Computer Society, Los Alamitos, CA, USA, 2023), pp. 177–183.

[44] G. Van de Stolpe, D. Kwiatkowski, C. Bradley, J. Randall, M. Abobeih, S. Breitweiser, L. Bassett, M. Markham, D. Twitchen, and T. Taminiau, Mapping a 50-spin-qubit network through correlated sensing, Nat. Commun. **15**, 2006 (2024).

[45] Y. Shen, P. Wang, C. T. Cheung, J. Wrachtrup, R.-B. Liu, and S. Yang, Detection of quantum signals free of classical noise via quantum correlation, Phys. Rev. Lett. **130**, 070802 (2023).

[46] D. D. Awschalom, R. Hanson, J. Wrachtrup, and B. B. Zhou, Quantum technologies with optically interfaced solid-state spins, Nat. Photonics **12**, 516 (2018).

[47] H. Bernien, B. Hensen, W. Pfaff, G. Koolstra, M. S. Blok, L. Robledo, T. H. Taminiau, M. Markham, D. J. Twitchen, L. Childress *et al.*, Heralded entanglement between solid-state qubits separated by three metres, Nature **497**, 86 (2013).

[48] A. Sipahigil, R. E. Evans, D. D. Sukachev, M. J. Burek, J. Borregaard, M. K. Bhaskar, C. T. Nguyen, J. L. Pacheco, H. A. Atikian, C. Meuwly *et al.*, An integrated diamond nanophotonics platform for quantum-optical networks, Science **354**, 847 (2016).

[49] L. Mineh and A. Montanaro, Accelerating the variational quantum eigensolver using parallelism, Quantum Sci. Technol. **8**, 035012 (2023).

[50] A. Kinos, D. Hunger, R. Kolesov, K. Mølmer, H. de Riedmatten, P. Goldner, A. Tallaire, L. Morvan, P. Berger, S. Welinski *et al.*, Roadmap for rare-earth quantum computing, arXiv:2103.15743.

[51] A. Bourassa, C. P. Anderson, K. C. Miao, M. Onizhuk, H. Ma, A. L. Crook, H. Abe, J. Ul-Hassan, T. Ohshima, N. T. Son *et al.*, Entanglement and control of single nuclear spins in isotopically engineered silicon carbide, Nat. Mater. **19**, 1319 (2020).

[52] M. Steiner, P. Neumann, J. Beck, F. Jelezko, and J. Wrachtrup, Universal enhancement of the optical readout fidelity of single electron spins at nitrogen-vacancy centers in diamond, Phys. Rev. B **81**, 035205 (2010).